First Results from the X–ray and Optical[1] Survey of the Chandra Deep Field South

R. Giacconi[1,2], P. Rosati [3], P. Tozzi[1,4], M. Nonino[4], G. Hasinger[5], C. Norman[1,6], J. Bergeron[3], S. Borgani[7], R. Gilli[1,8], R. Gilmozzi[3], and W. Zheng[1]

[1]Dept. of Physics and Astronomy, The Johns Hopkins University, Baltimore, MD 21218, USA

[2]Associated Universities Inc., 1400, 16th st. NW, Washington DC 20036, USA

[3]European Southern Observatory, Karl-Schwarzschild-Strasse 2, D-85748 Garching, Germany

[4]Osservatorio Astronomico di Trieste, via G.B. Tiepolo 11, I–34131, Trieste, Italy

[5]Astrophysikalisches Institut, An der Sternwarte 16, Potsdam 14482 Germany

[6]Space Telescope Science Institute, 3700 S. Martin Drive, Baltimore, MD 21210, USA

[7]INFN, c/o Dip. di Astronomia dell'Università, via Tiepolo 11, I–34131, Trieste, Italy

[8]Università degli Studi di Firenze, Dip. Astronomia, Largo E. Fermi 5, I-50125, Firenze, Italy

ABSTRACT

We present our first results from 130 ks of X–ray observations obtained with the Advanced CCD Imaging Spectrometer on the Chandra X–ray Observatory. The field of the two combined exposures is 0.096 square degrees and the detection limit is to a S/N ratio of 2 (corresponding to ~ 7 net counts). We reach a flux of 2×10^{-16} erg s^{-1} cm^{-2} in the 0.5–2 keV soft band and 2×10^{-15} erg s^{-1} cm^{-2} in the 2–10 keV hard band. Our combined sample has 144 soft sources and 91 hard sources respectively for a total of 159 sources. Fifteen sources are detected only in the hard band, and 68 only in the soft band.

For the optical identification we carried out a survey in VRI with the FORS–1 imaging-spectrometer on the ANTU telescope (UT–1 at VLT) complete to R$\leq$ 26. This dataset was complemented with data from the ESO Imaging Survey (EIS) in the UBJK bands and the ESO Wide Field Imager Survey (WFI) in the B band. The positional accuracy of the X–ray detections is of order of 1" in the central 6'. Optical identifications are found for $\simeq 90\%$ of the sources. Optical spectra have been obtained for 12 objects.

We obtain the cumulative spectra of the faint and bright X–ray sources in the sample and also the hardness ratios of individual sources. A power law fit in the range 2–10 keV using the galactic value of $N_H \simeq 8 \times 10^{19}$ cm^{-2}, yields a photon index of $\Gamma = 1.70 \pm 0.12$ and 1.35 ± 0.20 (errors at 90% c.l.) for the bright and faint sample respectively, showing a flattening of the spectrum at lower fluxes. Hardness ratio is given as a function of X–ray flux and confirms this result. The spectrum of our sources is approaching the spectrum of the XRB in the hard band, which has an effective $\Gamma = 1.4$.

---

[1]Based on observations performed at the European Southern Observatory, Paranal, Chile

Correlation function analysis for the angular distribution of the sources indicates that they are significantly clustered on scales as large as 100 arcsec. The scale-dependence of the correlation function is a power law with index $\gamma \sim 2$, consistent with that of the galaxy distribution in the local Universe. Consequently, the discrete sources detected by deep Chandra pointed observations can be used as powerful tracers of the large-scale structure at high redshift.

We discuss the LogN–LogS relationship and the discrete source contribution to the integrated X–ray sky flux. In the soft band, the sources detected in the field at fluxes below 10^{-15} erg s^{-1} cm^{-2} contribute $(4.0 \pm 0.3) \times 10^{-12}$ erg cm^{-2} s^{-1} deg^{-2} to the total XRB. The flux resolved in the hard band down to the flux limit of 2×10^{-15} erg s^{-1} cm^{-2}, contributes $(1.05 \pm 0.2) \times 10^{-11}$ erg cm^{-2} s^{-1} deg^{-2}. Once the contribution from the bright counts resolved by ASCA is included, the total resolved XRB amounts to 1.3×10^{-11} erg cm^{-2} s^{-1} deg^{-2} which is a fraction of 60–80% of the total measured background. This result confirms that the XRB is due to the integrated contribution of discrete sources, but shows that there is still a relevant fraction (at least 20%) of the hard XRB to be resolved at fluxes below 10^{-15} erg s^{-1} cm^{-2}.

We discuss the X–ray flux versus R magnitude relation for the identified sources. We find that $\simeq 10\%$ of the sources in our sample are not immediately identifiable at $R > 26$. For these sources $S_X/S_{opt} > 15$, whereas most of the ROSAT and Chandra sources have $S_X/S_{opt} < 10$. We have found also a population of objects with unusually low S_X/S_{opt} that are identified as galaxies. The R–K vs R color diagram shows that the Chandra sources continue the trend seen by ROSAT.

For our 12 spectroscopically studied objects with redshifts, we observe 4 QSOs, 5 Sy2 galaxies, 1 elliptical and 2 interacting galaxies. We compare the L_X vs z obtained with these measurements and show that Chandra is achieving the predicted sensitivity.

Subject headings: diffuse radiation – surveys – cosmology: observations – X–rays: galaxies – galaxies: active

1. INTRODUCTION

In the rocket flight which discovered X-ray stars (Giacconi et al 1962), the presence of a diffused X-ray background (XRB) was also observed. Reviews of the findings up to the middle 70's are given in Gursky and Schwartz (1977), Fabian and Barcons (1992) and references therein. The measurement by Uhuru of the high degree of isotropy led to the conclusion that the XRB had to be extragalactic. The logN–logS relation for sources at high galactic latitude ($b > 20$) showed a slope of 1.5 which would account for the entire XRB already at fluxes larger than 10^{-14} erg cm^{-2} s^{-1} (Matilsky et al 1973). The required number of discrete sources had to be large ($N > 10^6$ sr^{-1}) to be consistent with the value of the fluctuations of $< 3\%$ over 2 degrees (Schwartz et al 1976).

The spectrum of the XRB had been measured over the range 3 to 100 keV and could be fitted with two power laws of index $\Gamma = 1.4$ for $E < 25$ keV and $\Gamma = 2.4$ for $E > 25$ keV (Gursky and Schwartz 1977). However, the results of HEAO–1 gave an excellent fit over the $3 - 30$ keV range of the XRB spectrum to a thermal bremsstrahlung from a hot plasma at 40 keV, leading the authors (Marshall et al 1980) to suggest that the flux could be due to a hot intergalactic medium as had been considered by Field and Perrenod (1977). The finding that the spectrum of AGNs had been measured to be steeper than that of the XRB (Mushotzky 1984) further strengthened the view that the XRB could not be due to the sum of known sources.

On the other hand, the Einstein survey showed that about 25% of the soft XRB (1–3 keV) was resolved into discrete sources at a flux of order 3×10^{-14} erg s^{-1} cm^{-2} (Giacconi 1980, Griffiths et al. 1983). A large fraction of these sources were AGNs. A reasonable extrapolation of the X-ray properties and optical counts of extragalactic sources led to the conclusion that it was unlikely that discrete sources contributed less than 50% of the XRB (e.g., Schmidt & Green 1986; Setti 1985). If so, and their spectrum continued to be steep (energy index $\alpha \sim 0.7 - 1.2$), then one could show that a diffuse bremsstrahlung hypothesis for the residual was untenable (Giacconi & Zamorani 1987). The COBE result entirely ruled out the possibility that the XRB could be due to thermal bremsstrahlung from a hot plasma (Mather et al. 1990).

The ROSAT survey established that 70–80% of the XRB is resolved into discrete sources in the 1-2 keV range at a flux level of 1×10^{-15} erg s^{-1} cm^{-2} (Hasinger et al. 1998). At higher energies (2–10 keV) the ASCA and BeppoSAX satellites have achieved detection limits of $3 - 5 \times 10^{-14}$ erg s^{-1} cm^{-2} and have resolved $\sim 25\%$ of the 2-10 keV XRB into discrete sources (Ogasaka 1998; Cagnoni et al. 1998; Della Ceca et al. 1999a; Giommi, Fiore & Perri 1998). The population of sources appears to be composed of obscured and unobscured AGNs. The majority of hard sources appear to have counterparts in the soft X–ray band and are believed to be obscured AGNs. In this case, the soft emission may be due to electron scattered radiation. In addition to the scattered radiation, there are in principle several possibilities why obscured AGN could show up in the soft band: a very high redshift, so that the absorption cutoff is shifted to the soft energy band; a starburst component; photoionized gas emission (as observed by XMM in NGC 1068, Paerels 2000).

The very high sensitivity, broad energy range and high angular resolution of the Chandra

observatory (Weisskopf, O'dell & van Speybroeck 1996) will permit the final resolution of the origin of the XRB at least in the 0.5 to 10 keV range. However, the most important aspect of the deep surveys (exposure time $\simeq$ 1 Msec) to be conducted with Chandra will be the study of the individual classes of objects rather than their integrated properties. Based on the limiting sensitivity, exposure map and source surface density found in the first Chandra data, we expect a limiting flux of $f_{[0.5-2keV]} = 2 \times 10^{-17}$erg s^{-1} cm^{-2} in the center of the field for 1.5 Msec of exposure. Such a depth will permit the study of: (1) the formation and evolution of AGNs at large redshifts ($z \simeq 5$); (2) clusters of galaxies at redshifts greater than 2 and (3) study of star–forming regions in galaxies at moderate redshifts ($z \simeq 1$).

We selected a field for our observations which has the following properties: (1) very low Galactic neutral hydrogen column ($N_H \simeq 8 \times 10^{19}$cm^{-2}) – a Southern sky equivalent to the Lockman Hole; (2) no stars brighter than $m_v = 14$ and (3) well suited to observations with 8 meter class telescopes such as the VLT and Gemini. Our observations are centered at RA = 3:32:28.0 DEC = -27:48:30 (J2000). The results in this paper pertain to the initial 130 ksec of observations out of the currently planned 500 ksec (another exposure of 500 ksec has been approved, for a total of 1 Msec, for the end of the year 2000). The plan of the paper is as follows. In §2 we describe the data reduction. In §3 we will present the results on the X–ray data including spectral properties of the sources, number counts and correlation function. In §4 we will describe the optical data. In §5 we will discuss our results. Finally, we will summarize our conclusions in §6.

2.   X–RAY DATA: OBSERVATIONS AND DATA REDUCTION

The Chandra Deep Field South (CDFS) data are obtained from the combination of two exposures taken when the Advanced CCD Imaging Spectrometer–Imaging (ACIS-I) detector was at a temperature of -110 K. The first observation (Obs ID 1431_0) was taken on 1999-10-15/16, in the very faint mode, for a total 34 ks exposure. The second observation (Obs ID 1431_1) was taken on 1999-11-23/24, in the faint mode, for a total 100 ks exposure.

The data were reduced and analyzed using the CIAO software (release V1.3, see http://asc.harvard.edu/cda). The Level 1 data were processed using the latest calibration files and the latest aspect solution. We included the new quantum efficiency uniformity files, that correct the effective area for loss due to charge transfer inefficiency at a temperature of -110 K. This correction compensates for the loss of events far from the readout, especially at high energies, and it is particularly relevant when fitting the total spectrum in the broadest energy range.

The data were filtered to include only the standard event grades 0,2,3,4 and 6. All hot pixels and columns were removed as were also the columns close to the border of each node, since the grade filtering is not efficient in these columns. We looked for flickering pixels, defined as pixels with more than 4 events contiguous in time. The removal of columns and pixels reduces slightly the effective area of the detector and this effect has been included when computing the total exposure

maps. Time intervals with background rates larger than 3 sigma over the quiescent value (0.31 counts s^{-1} per chip in the 0.3–10 keV band) were removed. This procedure gave 25 ksec of effective exposure out of the first observation, and 93 ksec out of the second, for a total of 118 ks. The two observations had different roll angles, so that the exposure in the combined image of the field ranges between 25 and 118 ksec over a total coverage of 0.096 deg^2. Since the two observations have the same nominal aimpoint, the exposure time is 118 ksec over the majority of the field of view. The chip S–2 was active during both observations. We did not include data from this chip in the following analysis, since the point spread function (PSF) is very broadened ($\simeq$ 15 arcsec) and it adds a very small effective area especially at low fluxes.

We selected a soft band from 0.5–2 keV and a hard band from 2–7 keV in which to detect sources. The hard band was cut at 7 keV since above this energy the effective area of Chandra is decreasing, while the instrumental background is rising, giving a very inefficient detection of sky photons. A wavelet detection algorithm run on the 7–10 keV image, gives no sources over our detection threshold. Note also that the counts expected on the ACIS-I detector in the 7–10 keV band for the hardest sources, are always no more than 3% of the total hard photons. Thus, including the 7–10 keV band would always decrease the signal for the hard sources. However, we will always quote the fluxes in the canonical 2–10 keV band, as extrapolated from the flux measured from the 2–7 keV count rate, in order to have a direct comparison with the previous results.

Figure 1 shows a sky map of the field. We used a wavelet detection algorithm (Rosati et al. 1995) to find X–ray sources. In order to match the PSF variation as a function of the off-axis angle, the wavelet analysis was carried out at five scales, $a_i = (\sqrt{2})^i$ pixels, for $i = 0, 1, 2, 3, 4$ and pixel size 0.984 arcsec. Simulations have shown that simple aperture photometry is very accurate across the ACIS–I detector and was therefore preferred to time–consuming wavelet photometry (see Rosati et al. 1995). The area of extraction of each source is defined as a circle of radius $R_s = 2.4 \times FWHM$ (with a minimum of 5 pixels ($\simeq 5''$). The FWHM (in arcsec) is modeled as a function of the off-axis angle θ (in arcmin) as $FWHM(arcsec) = \sum_{i=0,3} a_i \theta^i$, with $a_i = \{0.678, -0.0405, 0.0535\}$ (see the Observatory Guide, http://asc.harvard.edu/udocs/docs/docs.html). The background was calculated locally for each source in an annulus with outer radius of $R_s + 8''$ and inner radius of $R_s + 2''$, after masking out other sources. With this choice, the average number of counts in the background regions is $\simeq$ 11–22 in the soft band and $\simeq$ 17–34 in the hard band. Thus the local estimate of the background has a poissonian fluctuation always less than 30%. We define the S/N ratio as $S/\sqrt{S + 2B}$ where S are the net counts in the extraction region of radius R_s, and B are the background counts found in the annulus defined above and rescaled to the extraction region. Since the lowest S/N ratio of our final catalog is 2 across the field, the flux threshold across the field in the soft band, including the effect of vignetting and of the point spread function, is $\simeq 2 \times 10^{-16}$ erg s^{-1} cm^{-2} within the central 6 arcmin, and grows to $\simeq 5 \times 10^{-16}$ erg s^{-1} cm^{-2} at 10 arcmin off–axis. In the hard band, the flux limit is $\simeq 2 \times 10^{-15}$ erg s^{-1} cm^{-2} within the central 6 arcmin, and $\simeq 4 \times 10^{-15}$ erg s^{-1} cm^{-2} 10 arcmin off–axis. In the following we describe the analysis of point–like sources only, leaving the analysis of diffuse sources to a subsequent paper.

We performed extensive simulations to determine the accuracy of our aperture photometry and our completeness limit. The aperure photometry with the aforementioned parameters is accurate within 3%. From the catalog of candidate sources selected by the wavelet detector, we remove all sources with a signal-to-noise ratio $S/N < 2$, corresponding to 7 net counts in the center. With these criteria, our detections have a less than 5% probability of including a fake source on the total ACIS-I field. This is a robust limit since the background is very low and we are always signal limited. More importantly, the simulations provide a test for the sky coverage model, which is defined as the area of the sky where a point–like source of a given flux can be detected by the wavelet algorithm and has a $S/N > 2$ in the extraction region of radius R_S. The effective solid angle of the Chandra observations is equal to the geometrical solid angle (0.096 deg^2) only at fluxes $> 2 \times 10^{-15}, 2 \times 10^{-14}$ erg s^{-1} cm^{-2} in the soft and hard bands respectively, whereas it drops at 50% of these values at fluxes $< 3.2 \times 10^{-16}, 2.3 \times 10^{-15}$ erg s^{-1} cm^{-2}. By comparing the input LogN–LogS with the output LogN–LogS in the simulations we verified that our model for the sky coverage is accurate within 5%. A further check comes from the preliminary analysis of a total exposure of 300 ksec of the CDFS. We found the presence of 5% of spurious sources, to be added to six sources associated with flickering pixels that were not removed from the exposure.

We used two separate conversion factors to derive the energy flux from the observed count rate for the soft and hard bands. The conversion factors were $(4.8 \pm 0.3) \times 10^{-12}$ erg s^{-1} cm^{-2} per count s^{-1} in the soft band, and $(2.7 \pm 0.3) \times 10^{-11}$ erg s^{-1} cm^{-2} per count s^{-1} in the hard band assuming an absorbing column of 8×10^{19} cm^{-2} (Galactic value) and a photon index, $\Gamma = 1.7$, consistent with the average spectrum of the bright sample. The uncertainties in the conversion factors reflect the range of possible values for the photon index, $\Gamma = 1.4 - 2.0$. As suggested by the spectral analysis of the stacked spectra, these values are representative of our sample (see §3.1). The conversion factors were computed at the aimpoint (which is the same for both exposures). Before being applied to the net count rate of a given sources, the conversion factors are corrected for vignetting. The correction is given by the ratio of the value of the exposure map at the aimpoint to the value of the exposure map at the source position (averaged over the extraction region). This is done separately for the soft and the hard band, using the exposure maps computed for energies of 1.5 keV (soft) and 4.5 keV (hard). Sources with more than 100 total counts in the two bands were analyzed also with XSPEC (Arnaud 1996), fitting an absorbed power law to the data binned with a minimum of 20 photons per bin. The soft and hard fluxes of the fitted spectra are always within 10% of the values obtained using the conversion factors quoted above.

3. X–RAY DATA: RESULTS

3.1. X–ray Spectra and Hardness Ratio

The majority of the sources are faint. Thus we measure the average stacked spectrum of both the faint sources and bright sources. To this purpose, we use only the longest exposure

(93 ksec), in order to have a uniform exposure for the stacked spectra. From our sample of 159 sources, 5 were excluded because they were present only in the field of view of the first exposure. We divided the remaining sample into two groups of 29 and 125 with a dividing count rate of 1.0×10^{-3} cts/sec in the total band 0.5–7 keV. The background spectrum was obtained using the event file of the total field of the same exposure, after the removal of the detected sources. The background is scaled by the ratio of the total exposure maps of the sources and of the background. Such a procedure guarantees a correct background subtraction despite the non-uniformities of the instrumental background across ACIS-I. The ancillary response matrix for the effective area is obtained from the counts–weighted average of the matrices of the single sources. The response matrix is assumed to be the one computed in the aimpoint. We recall that we use the quantum efficiency uniformity file appropriate for a temperature of -110 K. This file corrects the quantum efficiency with respect to the pre–flight values; especially, it takes into account the correction due to the charge transfer inefficiency.

We used XSPEC to compute the slope of a power law spectrum with N_H absorption at low energy, in the energy range 0.5–10 keV and in the 2–10 keV band only. The value of N_H is fixed at the galactic value when the fit is done using the hard energy range, while, if the total energy range is used, N_H is left free to vary. We exclude bins below 0.5 keV because the calibration is still uncertain below this energy.

For the total sample, including all the 154 sources on the largest exposure, we performed a power-law fit over the energy range 0.5–10 keV, and obtained a photon index Γ of 1.53 ± 0.07 and a column density $N_H = (6.0 \pm 3.0) \times 10^{20}$ cm^{-2}. Errors refer to the 90% confidence level. Then we perform the fit using only the 2–10 keV energy range, with Galactic $N_H = 8 \times 10^{19}$ cm^{-2}. We obtained $\Gamma = 1.61 \pm 0.11$. The contribution of the total sample to the XRB is $(4.0 \pm 0.3) \times 10^{-12}$ erg cm^{-2} s^{-1} deg^{-2} in the soft band and $(1.07 \pm 0.15) \times 10^{-11}$ erg cm^{-2} s^{-1} deg^{-2} in the hard band.

For the bright sample we obtained a photon index Γ of 1.71 ± 0.07 and $N_H = (7.0 \pm 2.0) \times 10^{20}$ cm^{-2} from the fit in the 0.5–10 keV energy range. Using the 2–10 keV energy range with galactic N_H we obtained Γ of 1.70 ± 0.12. The contribution of the bright sample to the XRB is $(6.3 \pm 0.9) \times 10^{-12}$ erg cm^{-2} s^{-1} deg^{-2} in the hard band.

We note that our bright sample shows a spectrum that is softer than that measured at about the same fluxes by ASCA in the energy range 2–10 keV (Della Ceca et al. 1999a find $\Gamma = 1.36 \pm 0.16$ at $S \simeq 6 \times 10^{-14}$ cgs, Ueda et al. 1999 find $\Gamma = 1.6$). This may be due to cosmic variance, since we poorly sample the bright end of the number counts.

For the faint sample we obtained a photon index Γ of 1.26 ± 0.10 and $N_H = (8.0 \pm 4.0) \times 10^{20}$ cm^{-2} from the fit using the 0.5–10 keV energy range, and Γ of 1.35 ± 0.20 with galactic N_H using the 2–10 keV energy range. The contribution of the faint sample in the hard band is $(4.3 \pm 1.0) \times 10^{-12}$ erg cm^{-2} s^{-1} deg^{-2}. In this case the spectral shape of the faint sample is consistent with the average spectrum of the XRB, which is around 1.4. We conclude that the average spectrum of the

detected sources is approaching the average shape of the hard background (see also Mushotzky et al. 2000).

The results of the spectral fits are shown in Table 1 and 2. The new quantum efficiency file provided with the CXC software was used which includes the effect of a reduced quantum efficiency at higher energies caused by the radiation damage.

To test the accuracy of our background subtraction, we perform the same spectral analysis in two ways. First, we build a synthetic spectrum using the software of M. Markevitch (see http://hea-www.harvard.edu~maxim/axaf/acisbg/) and we extracted the background from the same regions used for the extraction of the source spectra. In this way we eliminate the uncertainties due to the use of different extraction regions for the sources and the background. The results are the same within a few percent. Second, we build a background file summing all the background events found in the annuli around each source, and scaling the resulting file by the ratio of the total area af the extraction radius to the total area of the annuli. In this case too, the spectral fits change by a few percent.

A more detailed view of the spectral properties as a function of the fluxes comes from the hardness ratio $HR = (H - S)/(H + S)$ where H and S are the net counts in the hard (2–7 keV) and the soft band (0.5–2 keV), respectively. The distribution of the hardness ratios as a function of the count rate in the soft band is shown in Figure 2. There are 15 sources which are observed only in the hard band plotted at $HR = 1$ (corresponding to 9% of the total combined sample) and 68 which are observed only in the soft band, and are plotted at $HR = -1$. When the hardness ratio of the stacked spectrum of the only hard and only soft sources are computed, we find respectively $HR = 0.52 \pm 0.07$ and $HR = -0.65 \pm 0.05$. These hardness ratios are plotted as big asterisks. It is clear that faint sources are harder than bright ones, as already shown by the fits of the faint and bright stacked spectra.

We note that the stacked spectrum of the 15 sources detected only in the hard band, is consistent with the typical hardness ratio of the sources detected in both bands at the count rate of 10^{-4} cts/sec (see asterisks in the upper left of figure 2). In fact, we detected soft emission at 3 sigma levels in the stacked spectrum of these 15 sources. They have been missed in the soft band only because their emission were just below the detection threshold, while they would have been detected in a longer exposure. With this result, we have no evidence for sources in which the soft emission lower is lower than a 5–10 % of the energy emitted in the total (0.5–10 keV) band. This is expected in synthesis models of the XRB, where a soft component is considered in obscured AGNs.

3.2. LogN–LogS and Total Flux from Discrete Sources

We compute the number counts in the soft and hard bands. We show in Figure 3 a comparison of the soft 0.5–2 keV band to the ROSAT results. We find the Chandra results in excellent agreement with ROSAT in the region of overlap $S_{min} > 10^{-15}$ erg s^{-1} cm^{-2}. The Chandra data extend the

results to 2×10^{-16} erg s^{-1} cm^{-2}. In Figure 4 we show the LogN–LogS distribution for sources in the hard band, extending to a flux limit of 2×10^{-15} erg s^{-1} cm^{-2}, which represents a substantial improvement over previous missions.

We performed a maximum likelihood fit with a power law in the range $2 \times 10^{-16} < S < 3 \times 10^{-14}$cgs for the soft band and $2 \times 10^{-15} < S < 5 \times 10^{-14}$cgs in the hard band. The resulting best fit to the soft LogN–LogS is:

$$N(>S) = 370 \Big(\frac{S}{2 \times 10^{-15}} \Big)^{-0.85 \pm 0.15} \ sources deg^{-2} \tag{1}$$

and to the hard LogN–LogS:

$$N(>S) = 1200 \Big(\frac{S}{2 \times 10^{-15}} \Big)^{-1.0 \pm 0.20} \ sources deg^{-2} \tag{2}$$

The errors on the slope correspond to 2 sigma. The normalization of the soft counts is consistent within 1 sigma with the estimate of Mushotzky et al. (2000). On the other hand, we find that the previous Chandra results for the hard counts reported by Mushotzky et al. (2000), shown as crosses, are higher by 40% (see §5). From the maximum likelihood analysis we find that the normalization of the hard counts is, in fact, more than three sigma lower than the value found by Mushotzky et al. (2000). This is partially due to a different Γ used in deriving the converson factors. If we use an average $\Gamma = 1.4$, which is appropriate for the faint end of the number counts, the discrepance in normalization between our hard counts and that of Mushotzky et al. (2000) is reduced to 3 sigma. Our hard counts are consistent with those derived from other deep ACIS-I pointings, namely the Lynx Field (Stern et al. 2000, in preparation) and the HDF–N field (Garmire 2000, priv. communication), and in a completely independent fashion, from the first XMM deep surveys of the Lockman Hole (Hasinger et al. 2000, A&A, in press). In order to further investigate the difference with Mushotzky et al. results, a quantitative understanding of the clustering of X–ray sources on scales $\simeq 5$ arcmin would be needed, together with a knowledge of the sky coverage of that survey.

The integrated contribution of all sources within the flux range 10^{-13} erg s^{-1} cm^{-2} to 2×10^{-15} erg s^{-1} cm^{-2} in the 2-10 keV band is $(1.05 \pm 0.2) \times 10^{-11}$ erg s^{-1} cm^{-2} deg^{-2}. When this value is added to the contribution for fluxes $> 10^{-13}$ erg s^{-1} cm^{-2} from ASCA (Della Ceca et al. 1999b), we have a total contribution of $(1.3 \pm 0.2) \times 10^{-11}$ erg s^{-1} cm^{-2} deg^{-2}, which is close to the value 1.6×10^{-11} erg s^{-1} cm^{-2} deg^{-2} from UHURU and HEAO-1 (Marshall et al. 1980). More recent values of the 2–10 keV integrated flux from the BeppoSAX and ASCA surveys (e.g., Vecchi et al. 1999; Ishisaki et al. 1999 and Gendreau et al. 1995) appear higher by 20–40%. The integrated contribution of all sources in the field plus the bright sources seen by ASCA (data kindly provided by R. Della Ceca) is shown in Figure 5, together with the best estimates of the total background. The inclusion of the ASCA data at bright fluxes minimizes the effect of cosmic variance. We conclude that, given the uncertainty on the value of the total background, a fraction between 20% and 40% is still unresolved.

As for the total contribution to the soft X–ray background, we refer to the 1–2 keV band, following Hasinger et al. (1993, 1998) and Mushotzky et al. (2000). We find a contribution of $\simeq 5 \times 10^{-13}$ erg s^{-1} cm^{-2} deg^{-2} from discrete sources for fluxes lower than 10^{-15} erg s^{-1} cm^{-2}, corresponding to $\simeq 11\%$ of the unresolved flux (4.38×10^{-12} erg s^{-1} cm^{-2} deg^{-2}). If this value is summed to the contribution at higher fluxes (see Hasinger et al. 1998), we end up with a total contribution of $\simeq 3.5 \times 10^{-12}$ erg s^{-1} cm^{-2} deg^{-2} for fluxes larger than 2×10^{-16} erg s^{-1} cm^{-2}, corresponding to 80% of the unresolved value.

3.3. Angular Correlation Function

We have performed an analysis of the clustering of the X–ray sources in the CDFS using the sources which were identified in both the soft and hard bands. Since the limited statistics of our sample is expected to provide a weak clustering signal, we consider the average value of the two-point angular correlation function, $\bar{\omega}(\vartheta)$, defined as the excess of source pairs at separation $\leq \vartheta$ with respect to a random distribution (e.g., Peebles 1980). The random control sample was generated by distributing 50,000 points at random within an area of the sky with the same geometry as our field and a distribution modulated by the exposure map. Statistical errors in our value of $\omega(\vartheta)$ are estimated using the standard bootstrap resampling technique. The errors estimated with this technique are those due to statistical noise and do not include cosmic variance, which can only be assessed by repeating the analysis over several independent fields.

In Figure 6 we report the results for both the whole source population and for the subsample of 103 sources with fluxes $> 10^{-15}$ erg s^{-1} cm^{-2}. For reference, we also plot the power–law shape, $\bar{\omega}(\vartheta) = (\vartheta_c/\vartheta)^{1-\gamma}$, where $\gamma = 2$ is the slope of the spatial correlation function and $\vartheta_c = 10$ arcsec. Our analysis shows a statistically significant correlation signal out to scales of about 100 arcsec, while the noise dominates at larger separations. There is a marginal indication for the brighter sources to be more clustered at smaller separations. If confirmed, this would indicate that close pairs tend to be formed preferentially by bright objects, as is apparent even by visual inspection of the CDFS.

Vikhlinin & Forman (1995) analysed the correlation function for the the angular distribution of sources identified within ROSAT PSPC deep pointings. Quite remarkably, and despite the different nature of the sample they used, their correlation function turns out to be consistent with our Chandra data. Although their much larger statistics and the wider PSPC field–of–view allowed them to extend their analysis out to scales $\vartheta \simeq 800$ arcsec, the exquisite angular resolution achievable with Chandra provides here a detection of a correlation signal down to scales $\lesssim 10$ arcsec, about four times smaller than those sampled by Vikhlinin & Forman (1995).

We defer to a forthcoming paper a detailed correlation analysis for the distribution of the Chandra discrete sources and its implication for models aimed at explaining the nature of X–ray emission from AGNs.

4. OPTICAL AND NEAR–IR DATA

4.1. Imaging Survey Data

For identification of sources we have carried out an imaging survey in 3 bands, VRI with the FORS–1 camera at the ANTU telescope (UT–1 of VLT) (Programme Id 64.O–0621). We obtained exposures between 4000 to 7000 seconds in 4 adjacent fields of 6.8 x 6.8 arcmin^2 covering a large fraction of the CDFS 16x16 arcmin^2 field. Some shallower R-band fields of about 1200 seconds each in were obtained with the FORS imager in 4 additional positions in order to cover the entire area in the sky swept by different orientations of the Chandra field of view. For a few objects we were able to obtain spectroscopic information using the FORS–1 multislit capabilities in March 2000, just before the CDFSbecame inaccessible.

Our identification process was complemented with data from the ESO Imaging Survey (Rengelink et al. 1998) in the J and K bands obtained with SOFI at the NTT and in the UV bands obtained at the ESO NTT + SUSI–2. We also used a 30×30 arcmin image in B band obtained during the commissioning of the WFI camera at the ESO/MPI 2.2 meter telescope. The near-IR imaging covers, at present, the central 9.4×9.3 arcmin of the CDFS.

In the source identification process, we have found a positional offset of order of 0.3 arcsec and then found the correspondence of some of the brightest X–ray sources to likely candidates. We find an positional offset (-0.2, +1.4) arcsec between the optical and X–ray data. Using this correction we find X–ray/optical position deviations highly concentrated in a radius of rms 0.67 arcsec. A 2 arcesc correlation radius has been used for further analysis.

4.2. Optical counterparts of X–ray sources

Spatial coincidence allows identification of a large fraction of the sources. Approximately 10% of the X–ray sources with more than 10 detected counts have no immediately identifiable optical counterpart at $m_R < 26$. This could be due to a flux ratio S_X/S_{opt} larger than average but still close to the values observed for most of the sources (see Figure 7). We find approximately 1/3 of the sources are extended, which we associate with galaxies, and 2/3 of the sources appear are point like. If we compare the diagram of X–ray flux vs R magnitude for ROSAT (Hasinger et al. 1999) and the Chandra Deep Field South, we find that a large part of the Chandra sources appear to be consistent with an extension to fainter fluxes of the ROSAT sources, with an average $S_X/S_{opt} = 1$. However a significant fraction of the sample (10%) appear to have a very low $S_X/S_{opt} \leq 1/10$ and is detected only in the soft band at fluxes $< 10^{-15}$ erg s^{-1} cm^{-2}. Most of these objects are identified as galaxies. Another subsample of objects that have $S_X/S_{opt} \geq 10$, appear below fluxes $\simeq 3 \times 10^{-15}$ erg s^{-1} cm^{-2} (soft band). For these sources (about 20) with no optical counterpart at $R \simeq 26$, it could be that the corresponding objects are fainter, thereby increasing the S_X/S_{opt} to more than 10, or that they correspond to clusters.

We also plot R-K vs R magnitudes for the Chandra sources (see Figure 8). The color magnitude plot of the sources in the Chandra Deep Field South essentially overlaps the same plot with the ROSAT sources and extends to fainter magnitudes. The faintest Chandra sources appear to have very red colors, R–K $\simeq$ 5, with two of them at R–K $\geq$ 6, possibly indicating high redshift obscured AGNs.

4.3. Spectroscopic Information on Selected Sources

We have obtained spectroscopic data for a dozen optical counterparts of the X–ray sources using the multislit capability of FORS–1. The results are reported in Table 3, where we give the redshift, the counts in the soft and hard bands, the hardness ratio, the 0.5–2 keV X–ray flux in erg s^{-1} cm^{-2}, the 0.5–2 keV intrinsic luminosity in units of 10^{43} erg s^{-1} cm^{-2}, and the preliminary optical classification based on the width of the emission lines for Seyferts and QSOs. The objects described in Table 3 are not meant to be a well defined sample. They are just a random sample of bright CDFS sources for which we obtained the first spectra. The optical follow up started October 26 2000. At present we identify an elliptical galaxy where we observe an early type continuum with strong H and K absorption and weak, or no emission lines.

In total we identified 4 QSOs, 5 Seyfert 2 galaxies, 1 elliptical galaxy and 2 galaxies in an interacting pair. While we make no claim for completeness, it is interesting to note that the type of objects we observe are not extremely different from those we have observed in the ROSAT surveys. This can also be shown by plotting the computed values of L_X against z for the Chandra identifications (Figure 9). The many objects shown in the diagram are from previous surveys, as specified by different symbols. We note that the luminosity of the objects we have classified as QSOs is of order $1 - 7 \times 10^{43}$ erg s^{-1}, while the luminosity of those we classify as Seyfert 2 range between 10^{41} and 5×10^{43} erg s^{-1} cm^{-2}. The elliptical galaxy has a luminosity of 7×10^{40} erg s^{-1} and the nearby interacting pair galaxies have luminosities of 6 and 9×10^{39} erg s^{-1}. None of these objects appear to exhibit unusual properties.

5. DISCUSSION

From the sources detected in the Chandra Deep Field South we resolve 60–80% of the hard X–ray background. Their X–ray and optical properties are consistent with AGNs being the dominant population.

Absorbed AGNs, which have hard X–ray spectra, are missed in shallow surveys because of absorption dimming. They should be detected efficiently at low fluxes. The average spectrum of sources detected in X–ray surveys is expected to become harder with decreasing flux. This trend, which has already been observed in surveys performed with other satellites, is shown in Fig. 2.

Although the average spectrum of the sources gets harder with decreasing flux, only a small fraction ($\sim 9\%$) of the sources are detected in the hard band and not in the soft band. The hardness ratio of their stacked spectrum is consistent with the hardness ratios of the hard sources already detected both in the soft and hard bands, showing that they may lie just below the soft detection limit. This might imply that there is not a sizeable population of sources visible only in the hard band. Indeed, even in highly obscured AGNs, soft X–ray emission could be produced by partial covering of the nuclear emission, scattered components, or circumnuclear starbursts associated with AGN. Evidence for soft components in obscured AGNs is commonly observed in good quality X–ray spectra (e.g. Turner et al. 1997). Furthermore, the analysis of the X–ray color–color plot for recent ASCA and BeppoSAX surveys (Della Ceca et al. 1999b, Fiore et al. 2000, Giommi, Perri & Fiore, 2000) is consistent with this scenario, with the soft components being 1–10% of the nuclear emission.

For about 30% of the X–ray sources a host galaxy is resolved in the optical images. Most of the objects clustered on the lower–left corner of the soft S_X vs R diagram of Figure 7 are associated with bright galaxies. These galaxies are overluminous in the R band with respect to the other X–ray detected sources. Their X-ray emission generally comes from the center and is soft. Many of them are undetected in the hard band. The upper limits of the hardness ratios indicate that for the four brightest galaxies the average slope is $\Gamma \geq 1.5$. For three of these galaxies we have measured redshifts of z = 0.075, 0.075 and 0.215 with L_X of 9×10^{39}, 6×10^{39} and 7×10^{40} erg s^{-1} respectively as given in Table 3. The remainder of the galaxies are optically fainter and presumably more distant with luminosity greater than 10^{41} erg s^{-1}. All our soft galaxies fall below the detection threshold of the deepest ROSAT survey, 10^{-15} erg cm^{-2} s^{-1} (Hasinger et al. 1998), and thus Chandra has opened up a new parameter space for the study of moderate redshift galaxies in the X–ray band.

Two sources have been detected in the K but not in the R band (see Figure 8). They have R-K ≥ 6, and can be classified as Extremely Red Objects (EROs, Elston et al. 1988). Very red colors would be produced both by a dust reddened starburst or by an old stellar population in high redshift galaxies ($z \geq 1$, c.f. Crawford et al. 2000). In the first case the X–ray emission could arise from a surrounding cluster. Alternatively these objects could be high redshift obscured AGNs. The last hypothesis seems more likely for two objects with a similar color found by ROSAT in the Lockman Hole, based on their hard X-ray spectrum (Lehmann et al. 2000). However, the two EROs in our field are detected only in the soft band, suggesting that the X–ray emission is likely due to a starburst component or to a cluster. Another interesting possibility is that we are observing the soft scattered component in highly obscured Compton-thick AGNs at high redshift.

The cumulative number counts in the CDFS are fully consistent with those of Mushotzky et al. (2000) in the soft band, while in the hard band we found a surface density lower by $30 - 40\%$ depending on the average spectral slope Γ assumed for the X–ray source population. In the soft band the LogN-LogS is within the region allowed by ROSAT fluctuation analysis (Hasinger et al. 1993), while in the hard band the BeppoSAX fluctuation analysis (Perri & Giommi 2000) does not extend to sufficiently low fluxes to allow a full comparison. The source counts are in agreement

within the errors with the predictions of AGN synthesis models (Comastri et al. 1995, Gilli et al. 1999). Furthermore, the source density observed at low fluxes seems to favor models where the cosmological evolution of absorbed AGNs is faster than that of unabsorbed ones Gilli, Salvati & Hasinger (2000).

6.   CONCLUSIONS

In the Chandra Deep Field South we have a similarly large survey area and limiting flux to the Chandra Deep Field North carried out at Penn State. Our results are in general agreement with those quoted by this group who, in their two recent papers (Hornschemeier et al. 2000, Brandt et al. 2000), concentrated on a limited number (~ 10) of sources where they had optical identifications.

The limiting flux of the Mushotzky et al. (2000) results is similar but the area surveyed is about one third of the two Deep Fields. While we agree on the soft counts, we have a $\sim 40\%$ lower normalization of the hard counts, which implies that an important fraction of the XRB, at least 20%, has yet to be resolved.

Our data confirm that the XRB is due to the summed contribution of individual sources. In the 0.5–2 keV band this result had been foreshadowed by the Einstein measure of an individual source contribution of 25% (Giacconi 1980) and by the ROSAT determination of a 70% contribution (Hasinger et al. 1998). At higher energies (2–10 keV) the contribution to the background from sources was of 25% (Cagnoni et al. 1998; Della Ceca et al. 1999a; Ueda et al. 1999; Giommi, Fiore & Perri 1998). Our results bring the individual source contribution to the XRB in the 2–10 keV range to the level of 60–80%. Since there is still a non-negligible fraction of order 20-40% of the XRB to be resolved, it is important to push the detection limit at least down to 5×10^{-16} erg s^{-1} cm^{-2} in the hard band, or even at lower fluxes if the number counts flatten below 10^{-15} erg s^{-1} cm^{-2}.

With our increased number of sources we determined that the hardness ratio increases with fainter limiting flux and the spectrum of the fainter sources matches the background. Much of this was expected from earlier work of Setti and Woltjer (1989), Schmidt and Green (1986), Madau, Ghisellini & Fabian (1993), Comastri et al. (1995), and the ASCA results by Della Ceca et al. (1999a).

In addition, the angular correlation function of the X–ray sources in our field exhibits significant power on scales of order of the survey size. The slope and correlation length is consistent with that observed for galaxies. This indicates the presence of large–scale clustering at high redshift, whose spatial extent requires knowing the redshift distribution of the identified sources, by either spectroscopic or photometric methods. Detailed analyses of the correlation function in Chandra deep pointings will provide important complementary information on the nature of the discrete X-ray sources (e.g., Haiman & Hui 2000, and references therein).

Only 9% of the sources are detected in the hard band and not in the soft band. Most of these sources show some flux in the soft band below our detection threshold. As discussed in §3.1, the average hardness ratio of these faint sources is $HR = 0.52 \pm 0.07$ consistent with that found for the faint end of the sample. We conclude that we find no evidence for sources which are completely obscured in the X–ray soft band.

Our colour-magnitude and flux–magnitude diagrams follow the trends well known from the ROSAT data. A small fraction of the X–ray sources ($< 10\%$) with more than 10 detected counts are not immediately identified at R < 26.

A substantial number of nearby galaxies appear in the Chandra survey at very low S_x/S_{opt} and below the detection threshold of ROSAT. The X–ray emission from these galaxies is characterized by a soft spectrum and thus does not contribute significantly to the X–ray background at high energies. However, their study is of great intrinsic interest for the understanding of the properties and evolution of normal and starburst galaxies.

Chandra sensitivity is higher than or equal to that anticipated. Longer exposures to the confusion limit will still be in a signal–limited regime. For a 2×10^6 s exposure we should reach $S_{min} \sim 10^{-17}$ erg s^{-1} cm^{-2} in the soft band, which would allow detection of $L_X = 5 \times 10^{40}$ erg s^{-1} cm^{-2} at $z \sim 0.5$. This will enable a statistically significant study of normal and star–forming galaxies to significant look back times. Studies of bright QSOs can reach very large redshifts (5–10) and even observations of low surface brightness features (e.g., clusters) can be extended to $z \approx 3$.

A deep observation of 385 ksec in the same field is planned during the guaranteed time of one of us with XMM. The larger area of XMM will contribute significantly to the study of the spectra of point sources and the study of diffuse emission from galaxy clusters.

REFERENCES

Arnaud, K. A. 1996, in ASP conf. Series 101, Astronomical Data Analysis Software and Systems v, ed. G. Jacoby & J. Barnes, (San Fransisco: ASP), 17

Barrow, J.D., Sonoda, D.H., & Bhavsar, S.P. 1984, MNRAS, 210, 19

Brandt, W.N., et al. 2000, AJ, 119, 2349

Cagnoni, I., Della Ceca, R., & Maccacaro, T. 1998, ApJ, 493, 54

Comastri, A., Setti, G., Zamorani, G., & Hasinger, G. 1995 A& A, 296, 1

Crawford, C. S., Fabian, A. C., Gandhi, P.,Wilman, R. J., Johnstone, R. M. 2000, MNRAS submitted, astro-ph/0005242

Della Ceca, R., Castelli, G., Braito, V., Cagnoni, I. & Maccacaro, T. 1999a, ApJ, 524, 674

Della Ceca, R., Braito, V., Cagnoni, I. & Maccacaro, T. 1999b, astro-ph/9912016

Elston R., Rieke G. H., Rieke M., 1988, ApJ, 331, L77

Fabian. A., Barcons, X. 1992, ARA&A, 30, 429

Field, G.B., & Perrenod, S.C. 1977, ApJ 215, 717

Fiore, F., Giommi, P., Vignali, C., Comastri, A., Matt G., Perola, G. C., La Franca, F., Molendi, S., Tamburelli F., Antonelli A., 2000, MNRAS, submitted

Gendreau, K.C., et al. 1995 Publ. Astron. Soc. Jpn. 47, L5-L9

Giacconi, R., in "X–ray Astronomy" Proceedings of the Advanced Study Institute, Erice, Italy, July 1-14, 1979. Dordrecht, D. Reidel Publishing Co., 1980, p. 385-398

Giacconi, R., Gurksy, H., Paolini, F.R., & Rossi, B.B., 1962, Phys. Rev. Letters, 9, 439

Giacconi, R., & Zamorani, G., 1987, ApJ, 313, 20

Gilli, R., Risaliti, G., Salvati, M., 1999, A&A, 347, 424

Gilli, R., Salvati, M., & Hasinger, G. 2000, A&A, in press, astro-ph/0011341

Giommi, P., et al. 1998, In: The Active X–ray Sky: Results from Beppo SAX and Rossi-XTE, Nucl. Phys. B Proc. Suppl., 69, 591

Giommi, P., Fiore, F., & Perri, M. 1998 in Proceedings of the 3rd Integral Workshop, (ESA Press, Noorwijk), astro-ph/9812305

Giommi, P., Perri, M., Fiore, F. 2000, A&A in press, astro-ph/0006333

Griffiths, R.E., Murray, S.S., Giacconi, R., Bechtold, J., Murdin, P., Smith, M., MacGillivray, H.T., Ward, M., Danziger, J., Lub, J., Peterson, B.A., Wright, A.E., Batty, M.J., Jauncey, D.L., & Malin, D.F. 1983, ApJ, 269, 375

Gursky H and Schwartz D.A., 1977, Ann. Rev. Astron. and Astrophys., 15, 541-568

Haiman, Z., & Hui, L. 2000, ApJ, submitted (astro-ph/0002190)

Hasinger, G., Burg, R., Giacconi, R., Hartner, G., Schmidt, J., Truemper, J., & Zamorani, G. 1993, A&A 275, 1

Hasinger, G., Burg, R., Giacconi, R., Schmidt, J., Truemper, J., & Zamorani, G. 1998, A&A 329, 482

Hasinger, G., et al. 1999, in "Highlights in X-ray Astronomy", MPE report 272, p. 199, astro-ph/9901103

Hasinger, G., et al. 2000, A&A in press, astro-ph/0011271

Hornschemeier, A.E., et al. 2000, astro-ph/0004260

Ishisaki, Y., Makishima, K., Takahashi, T., Ueda, Y., Ogasaka, Y., & Inoue, H. 1999, ApJ submitted

Lehmann, I., Hasinger, G., Schmidt, M., Gunn, J. E., Schneider, D. P., Giacconi, R., McCaughrean, M., Trümper, J., Zamorani, G. 2000, A&A, 354, 35

Madau, P., Ghisellini G., & Fabian, A. C. 1993, ApJ, 410, L7

Marshall, F. et al. 1980, ApJ, 235, 4

Matilsky, T., Gursky, H., Kellog, E., Tananbaum, H., & Giacconi, R. 1973, ApJ, 181, 753

Mather, J.C., et al. 1990, ApJL, 354, L37

Mushotzky, R.F. 1984, Advances in Space Research, 3, n. 10-13, 157

Mushotzky, R.F., Cowie, L.L., Barger, A.J., & Arnaud, K.A. 2000, Nature, 404, 459

Ogasaka, Y. 1998, in "The hot universe", edited by Katsuji Koyama, Shunji Kitamoto, Masayuki Itoh (Dordrecht : Kluwer Academic) 188, 469

Paerels, F. et al. 2000, American Astronomical Society, HEAD meeting 32, 1.05

Peebles, P.J.E. 1980, The Large-Scale Structure of the Universe (Princeton: Princeton University Press)

Perri, M., Giommi, P., 2000, A&A Letters, in press, astro-ph/0006298

Rengelink R. et al. 1998, preprint, astro-ph/9812190

Rosati, P., Della Ceca, R., Burg, R., Norman, C., Giacconi, R. 1995, ApJL, 445, 11

Schmidt, M. & Green, R.F., 1986, ApJ, 305, 68

Schwartz, D.A., Murray, S.S., Gursky, H. 1976, ApJ, 204, 315

Setti, G., 1985 in "Nonthermal and Very High Temperature Phenomena in X–ray Astronomy", ed. Perola, G.C., & Salvati, M. (Rome: Instituto Astronomia, Università La Sapienza), p. 159

Setti, G. & Woltjer, L. 1989, A&A, 224, L21

Stern, D., et al. 2001, in preparation

Turner, T. J., George, I. M., Nandra, K., Mushotzky, R. F., 1997, ApJS, 113, 23

Ueda, Y., et al. 1999, ApJ, 518, 656

Vecchi, A., Molendi, S., Guainazzi, M., Fiore, F., & Parmar, A.N. 1999, A&A, 349, 73

Vikhlinin, A., & Forman, W. 1995, ApJ, 455, L109

Weisskopf, M. C., O'dell, S.L., van Speybroeck, L.P. 1996, SPIE, 2805, 2

Sample	Objects	Net Counts	Γ	N_H 10^{19} cm^{-2}	flux (2-10 keV) cgs deg^{-2}	χ^2/ν
total	154	10100	1.61 ± 0.11	8 (galactic)	$(1.07 \pm 0.15) \times 10^{-11}$	1.48
bright	29	6050	1.70 ± 0.12	8 (galactic)	$(6.3 \pm 0.9) \times 10^{-12}$	1.14
faint	125	4050	1.35 ± 0.20	8 (galactic)	$(4.3 \pm 1.0) \times 10^{-12}$	1.21

Table 1: Spectral fits on the 2–10 keV energy range.

Sample	Objects	Net Counts	Γ	N_H 10^{20} cm^{-2}	flux (0.5-2 keV) cgs deg^{-2}	χ^2/ν
total	154	10100	1.53 ± 0.07	6 ± 3	$(4.0 \pm 0.3) \times 10^{-12}$	1.48
bright	29	6050	1.71 ± 0.07	7 ± 2	$(2.9 \pm 0.2) \times 10^{-12}$	0.99
faint	125	4050	1.26 ± 0.10	8 ± 4	$(1.0 \pm 0.1) \times 10^{-12}$	1.18

Table 2: Spectral fits in the 0.5–10 keV energy range.

z	cts 0.5-2 keV	cts 2-7 keV	HR	S_X (erg/s/cm^2) 0.5-2 keV	L_X (10^{43} erg/s) 0.5-2 keV	Opt Id
2.750	21.7	15.9	-0.15	$6.4\ 10^{-16}$	3.6	BALQSO
0.545	1162	308.5	-0.58	$3.3\ 10^{-14}$	5.2	Sy2
1.218	135.5	46.6	-0.49	$3.9\ 10^{-15}$	3.5	QSO
0.430	44.4	0	-1.00	$1.2\ 10^{-15}$	0.12	Sy2
0.291	135.3	48.4	-0.47	$3.9\ 10^{-15}$	0.17	Sy2
0.075	12.3	0	-1.00	$3.5\ 10^{-16}$	0.00088	Inter. pair
0.075	9.1	0	-1.00	$2.3\ 10^{-16}$	0.00059	Inter. pair
0.215	9.8	0	-1.00	$3.1\ 10^{-16}$	0.0068	Ell
0.260	11.9	0	-1.00	$3.3\ 10^{-16}$	0.011	Sy2
1.180	55.4	21.3	-0.44	$1.6\ 10^{-15}$	1.3	QSO
0.490	90.8	29.9	-0.50	$2.6\ 10^{-15}$	0.33	Sy2
1.850	114.1	34.0	-0.54	$3.2\ 10^{-15}$	7.5	QSO

Table 3: Sources with optical spectra.

Figure cdfs130ksec.jpg

Fig. 1.— The Chandra Deep Field in the total band 0.5–10 keV (binned 2x2, pixel=0.984").
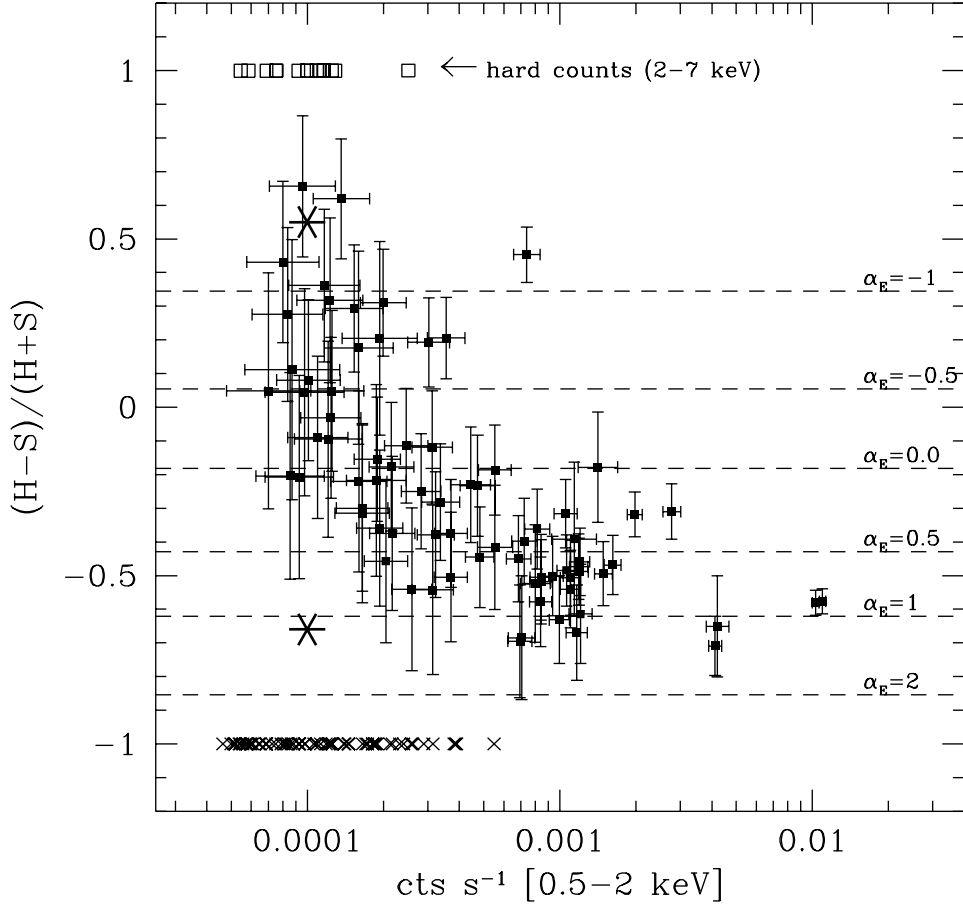
Fig. 2.— Hardness ratio as a function of the soft count rate for the sources detected in both bands. Sources detected only in hard (HR= 1) are shown with squares, the ones detected only in the soft (HR= −1) are shown with crosses. The two asterisks are the hardness ratio of the stacked spectra of the hard and soft sources. Dashed lines are power–law models with different energy index (α_E) computed assuming the galactic value $N_H \simeq 8 \times 10^{19}$ cm^{-2} and convoluted with a mean ACIS-I response matrix at the aimpoint.
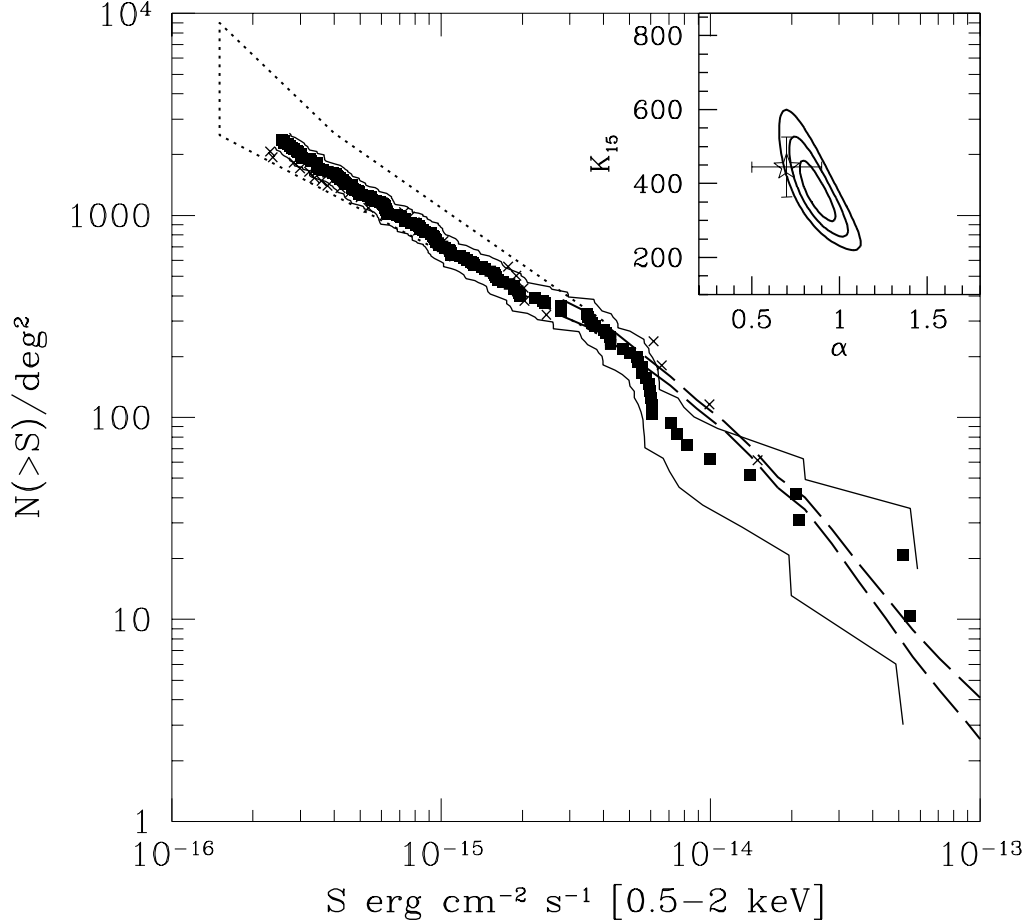
Fig. 3.— The LogN–LogS in the soft band from the Chandra Deep Field (filled squares). The crosses are from Mushotzky et al. (2000). Dashed lines are the counts from the Lockman Hole (Hasinger et al. 1998), and the dotted contour is the extrapolation from the fluctuation analysis in ROSAT data (Hasinger et al. 1993). The upper and lower solid lines indicate uncertainties due to the sum of the Poisson noise (1 σ) with the uncertainty in the conversion factor (see text). The insert shows the maximum likelihood fit to the parameters in the LogN–LogS fit $N(> S) = K_{15}(S/2 \times 10^{-15})^{-\alpha}$. The contours correspond to 1σ, 2σ and 3σ. The star is the fit from Mushotzky et al. (2000) at $S = 2 \times 10^{-15}$ erg s^{-1} cm^{-2}; the error bar is their quoted 68 % confidence level.
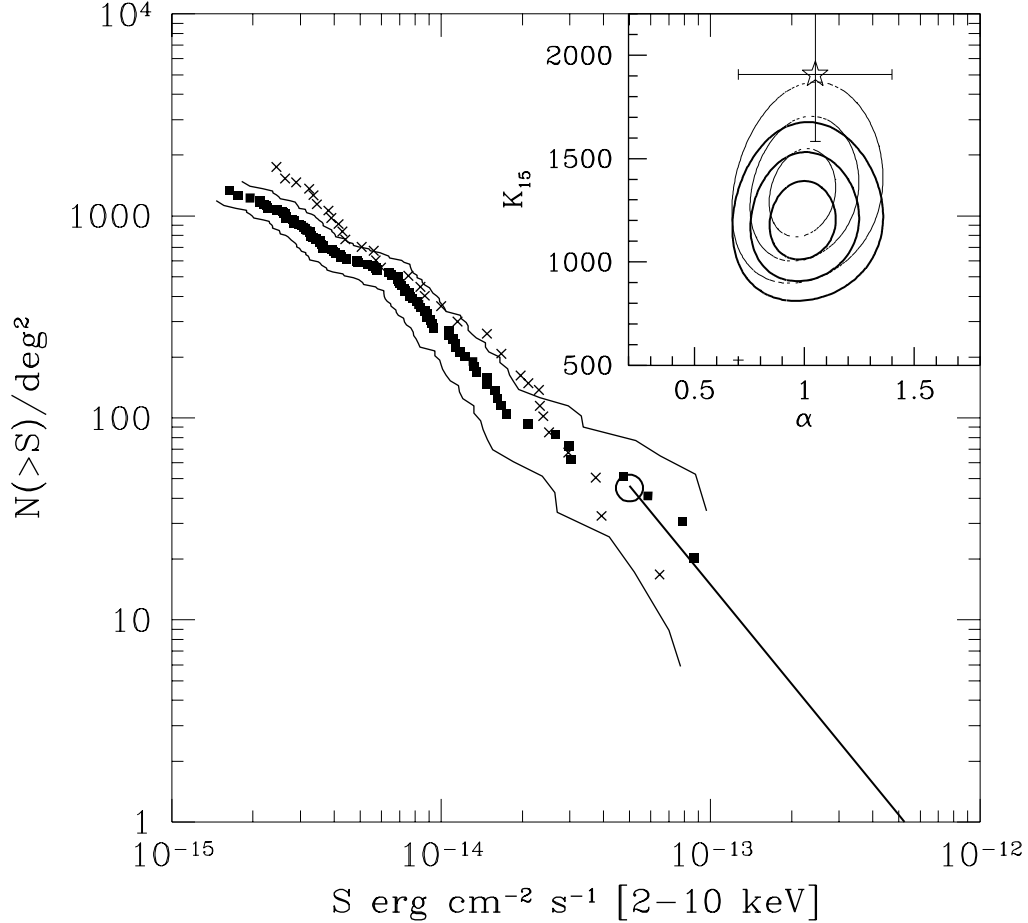
Fig. 4.— The LogN–LogS in the hard band from the Chandra Deep Field, symbols as in Figure 3. The open circle at high fluxes is from ASCA and Beppo SAX (Giommi et al. 1998, Ueda et al. 1999) and the continuous line is the fit to the counts from ASCA in the range $10^{-12} - 10^{-13}$ erg cm^{-2} s^{-1} (Della Ceca et al. 1999b). The upper and lower solid lines indicate uncertainties due to the sum of the Poisson noise, 1 σ, with the uncertainty in the conversion factor (see text). The insert shows the maximum likelihood fit to the parameters in the LogN–LogS fit $N(> S) = K_{15}(S/2 \times 10^{-15})^{-\alpha}$. The thick contours correspond to 1σ, 2σ and 3σ and use an average photon index of $\Gamma = 1.7$. The fainter countours use an average photon index of $\Gamma = 1.4$. The star is the fit from Mushotzky et al. (2000) at $S = 2 \times 10^{-15}$ erg s^{-1} cm^{-2}; the error bar is their quoted 68 % confidence level.
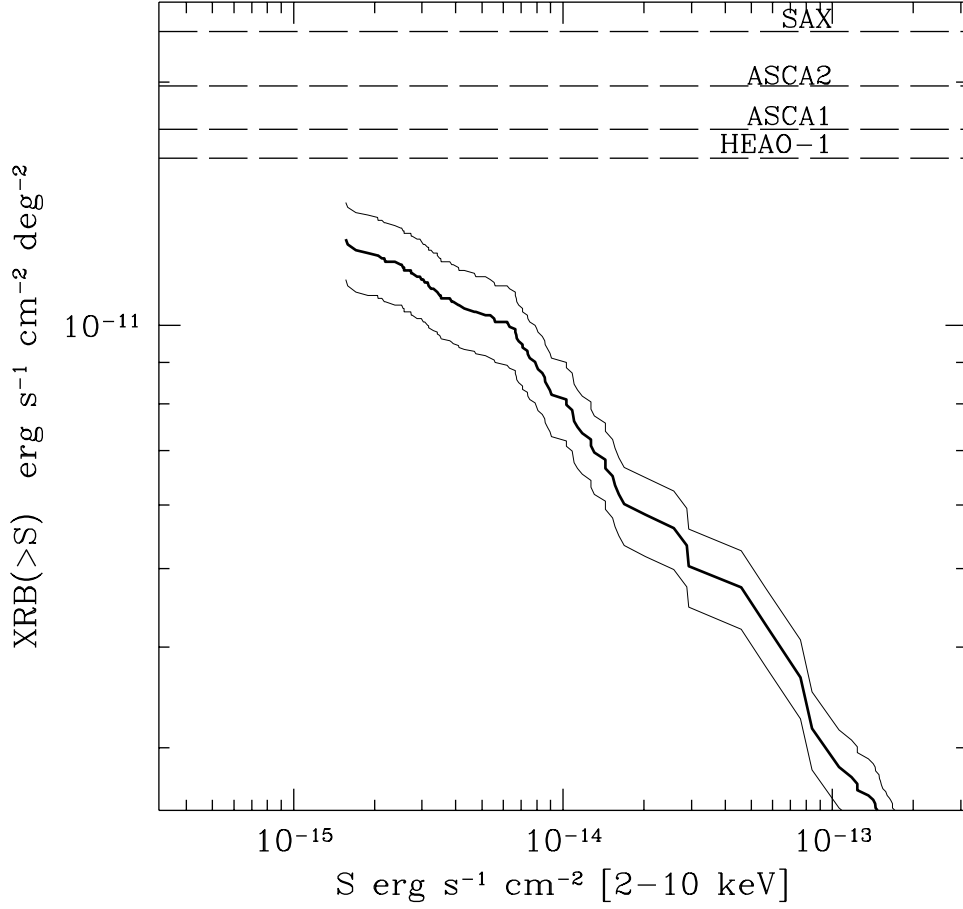
Fig. 5.— The contribution to the hard X–ray flux density as a function of the flux of the resolved sources. The total resolved contribution is computed from the CDFS sample plus the bright sample from ASCA at fluxes larger than $\simeq 10^{-13}$ (Della Ceca et al. 1999b). The upper dashed lines refer to previous measures of the hard X–ray background; from bottom to top: Marshall et al. (1980, HEAO-1), Ueda et al. (1996, ASCA1), Ishisaki (1999, ASCA2), Vecchi et al. (1999, BeppoSAX).
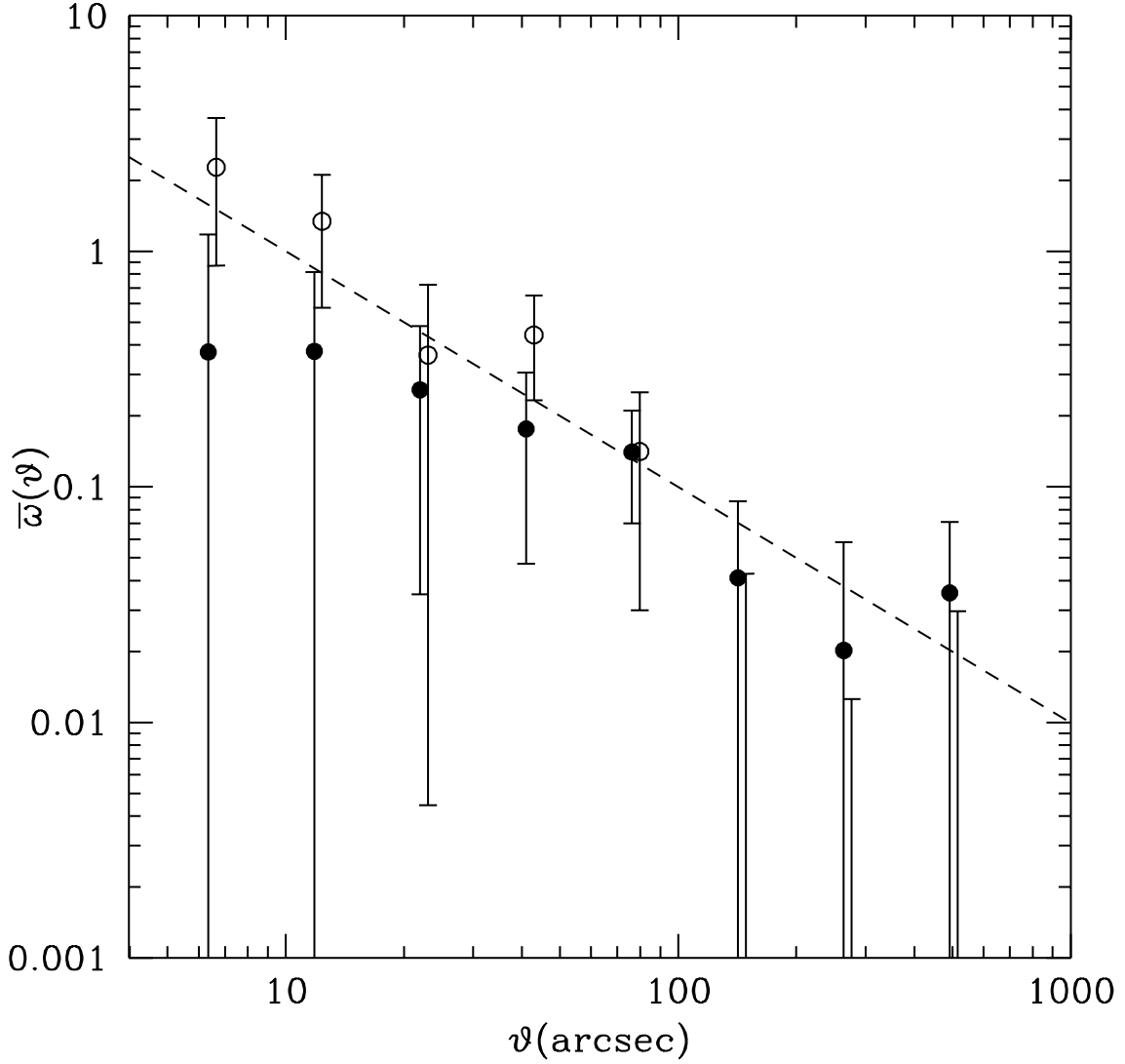
Fig. 6.— The average correlation function within the angular separation ϑ for the projected distribution of discrete sources identified within the CDFS. Filled circles refer to the whole sample, while open circles are for the subsample with total flux $S \geq 10^{-15}$ erg s^{-1} cm^{-2}. Errorbars are the 1σ scatter estimated over an ensamble of 2000 bootstrap samples (e.g., Barrow et al. 1984). For reasons of clarity, the open circles have been slightly shifted along the x-axis. The dashed line shows the power law shape, $\omega(\vartheta) = (\vartheta/\vartheta_c)^{1-\gamma}$, with $\gamma = 2$ and $\vartheta_c = 10$ arcsec.
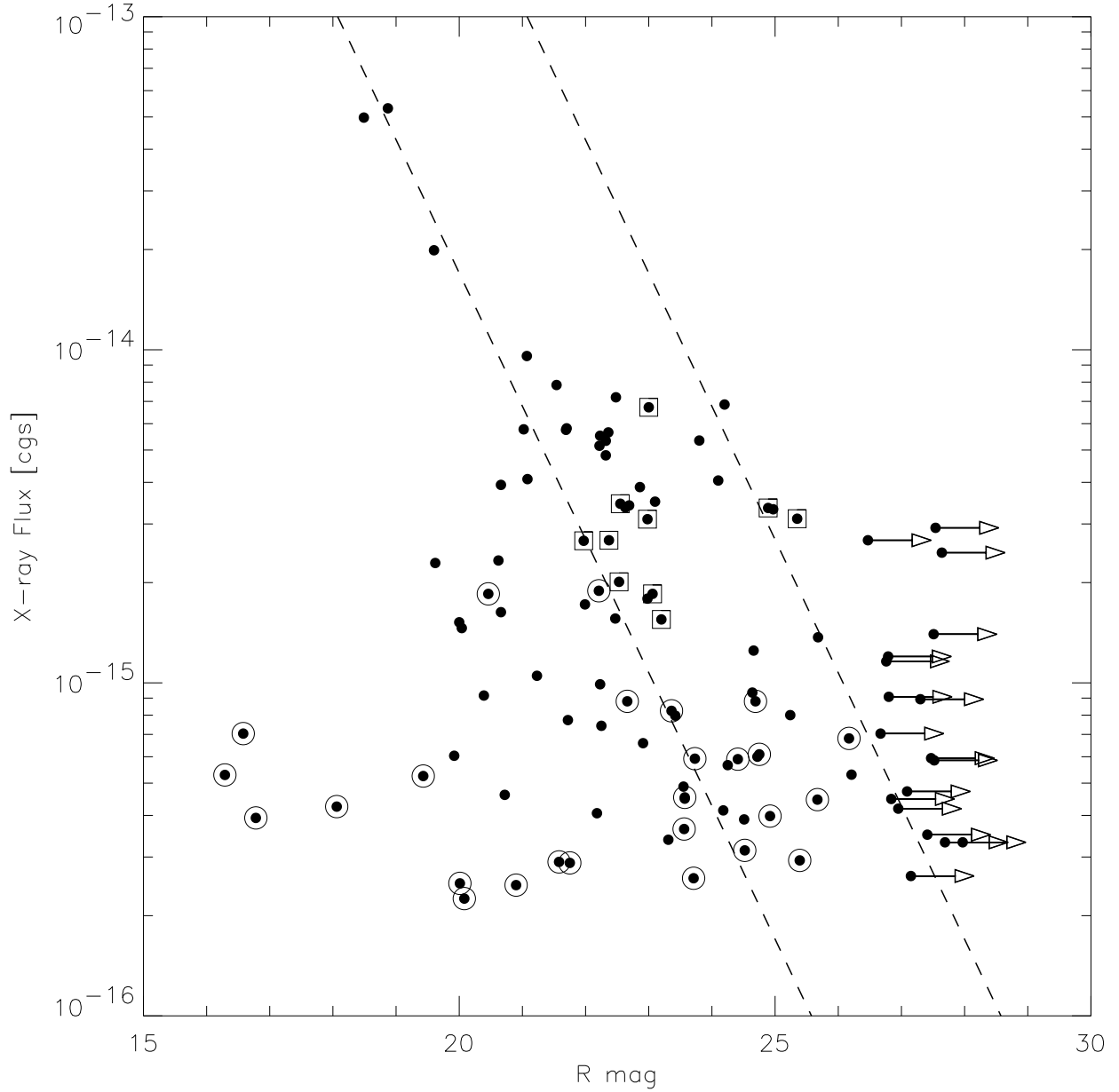
Fig. 7.— X–ray flux in the soft band versus optical R magnitude for Chandra sources (dots). The dotted circles correspond to sources detected only in the soft band. The dotted squares correspond to sources detected only in the hard band. The left dashed line marks a constant X–ray to optical flux ratio of 1, which is the best fit shown by Hasinger et al. (1998) for the ROSAT deep Survey. The right dashed line corresponds to an optical flux three magnitudes fainter ($S_X/S_{opt} > 15$). For the objects without optical counterpart, we put a 3σ lower limit to the magnitude (arrows). Note that below $F = 10^{-15}$ erg s^{-1} cm^{-2}, some sources depart more than three magnitudes from the $S_X/S_{opt} = 1$ relation.
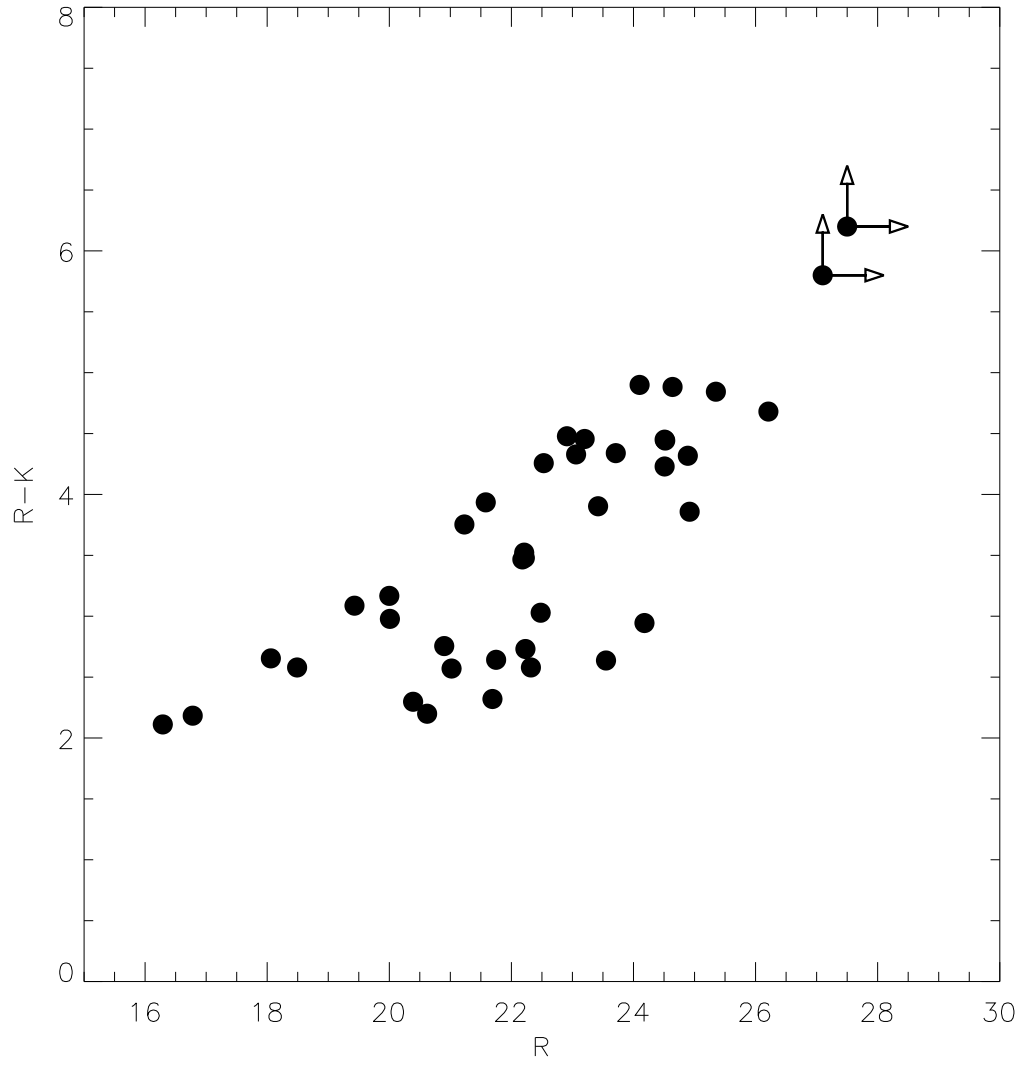
Fig. 8.— Color-magnitude diagram between R magnitude and R-K color for Chandra sources. The two upper right points are X–ray counterparts detected only in the hard band.
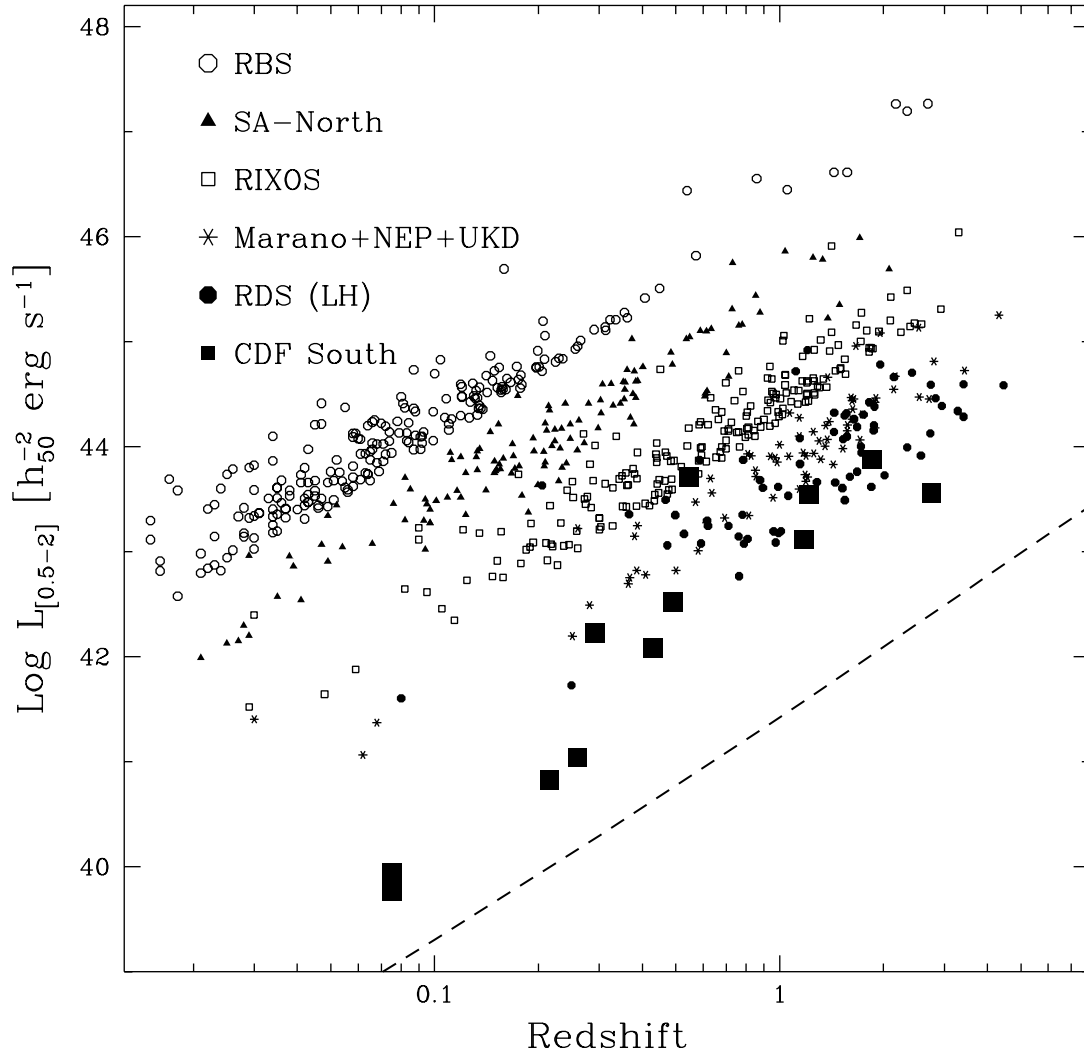
Fig. 9.— L_X in the soft band versus redshift for the Chandra sources (large squares), compared with previous surveys (as shown by the different symbols). The dashed line corresponds to a flux limit of 5×10^{-17} erg cm^{-2} s^{-1}.

This figure "cdfs130ksec.jpg" is available in "jpg" format from:

http://arXiv.org/ps/astro-ph/0007240v2